



Effect of axial ultrasonic vibration on the surface topography and microstructure of Al6061 chip in extrusion cutting

Yunyun Pi¹ · Chongjin Gao¹ · Xiaolong Yin²

Received: 15 April 2024 / Accepted: 21 May 2024 / Published online: 6 June 2024
© The Author(s), under exclusive licence to Springer-Verlag France SAS, part of Springer Nature 2024

Abstract

In this study, a new process of axial ultrasonic vibration-assisted extrusion cutting (AUV-EC) is proposed to prepare Al6061 alloy ultrafine-grained chip strips. The principles of AUV-EC are analyzed. The cutting motion trajectory equations of the main tool and the constraint tool during the AUV-EC process are established, and the theoretical cut marks on the chip surface are predicted. AUV-EC experiments are conducted to verify the theoretical cut marks on the chip surface and characterize the surface topography and microstructure of the chip strip samples. The results show that applying ultrasonic vibration with a frequency of 33~34.5 kHz and an amplitude of 1~6 μm in the AUV-EC process can improve the chip strip's surface quality. Compared with traditional extrusion cutting (EC) chip samples, AUV-EC chip samples have better surface flatness and smoothness and lower surface defect ratios. The average grain sizes of the traditional EC and AUV-EC chip samples are approximately 164 nm and 135 nm, respectively. Many dynamic recovery grains are distributed in traditional EC chips, but there is only a small amount in AUV-EC chips. The x-ray diffraction (XRD) test finds that the AUV-EC chip has a higher dislocation density.

Keywords Axial ultrasonic vibration-assisted extrusion cutting · Surface topography · Surface quality · Microstructure

Introduction

The technology of preparing ultrafine and nanocrystalline materials by large plastic deformation has been a popular research issue in recent years, such as in equal channel angular extrusion (ECAE) [1], high-pressure torsion (HPT) [2], upsetting [3], and extrusion cutting (EC) [4, 5]. Among these, the EC method does not require special equipment and can be processed on an ordinary lathe, and it can turn chips into valuable items. The advantages of the prepared strips are that they are regular in shape and that the grain size reaches the level of ultrafine crystals and nanocrystals, which have been a focus of research.

Researchers have done much research on EC. Sevier et al. established a simulation model for EC and predicted the

magnitude and change of equivalent strains under different chip compression ratios [6]. Bai et al. conducted an EC experiment and measured the grain size of the Al6013-T6 strip by EC, and they found that the grain size on the surface of the strip was smaller than that at the center [7]. P. Iglesias et al. studied the wear mechanism of oxygen-free copper and pure titanium nanostrips prepared by the EC process and found that under the same conditions, the wear rate of oxygen-free copper and pure titanium nanostrips was lower than that of ordinary oxygen-free copper and pure titanium. The wear rate decreased as the chip compression ratio decreased [8]. Dinakar Sagapuram et al. applied EC technology to magnesium alloys and found that continuous sheet-like ultrafine-grained magnesium alloys could be successfully prepared without preheating [9]. In EC, the smaller the chip compression ratio is, the greater the plastic deformation of the material and the better the grain size refinement effect; however, the performance of the material determines the minimum chip compression ratio. Klenosky et al. found that the chip compression ratio and cutting speed greatly influence the second shear zone. When the chip compression ratio decreased, the EC process became very unstable, and the strip edge appeared curled [10]. The

✉ Yunyun Pi
10698@sdpt.edu.cn

¹ College of Intelligent Manufacturing, Shunde Polytechnic, Shunde 528300, China

² College of Mechatronic Engineering, Zhongyuan University of Technology, Zhengzhou 451191, China

chip strips prepared by EC have better subsequent processing capabilities and potential industrial application value. For example, ultrafine-grained pure titanium can be processed into cylindrical dental micro-implants with threaded structure on the surface, which can replace the tooth roots by placing micro-implants in the frontal bone at the site of missing teeth through implant surgery [11]. In the field of equipment manufacturing, the research team of Purdue University successfully made ultrafine-grained chip into core material of golf balls [12]. Some scholars have processed EC chips and its size grade of ultrafine-grained materials into micro vascular stents [13], micro gears [14] and micro bolts [15].

In the process of large plastic deformation, the heat generated by plastic deformation and friction work will damage the surface quality and mechanical properties of the material. Therefore many researchers have combined other technologies with large plastic deformation technology to form new large plastic deformation processing technology in recent years. Yin combined low-temperature treatment with EC. The study found that the surface quality of the Al7075 strip prepared with liquid nitrogen treatment was better than that of the Al7075 strip designed at room temperature, with a smaller grain size and greater Vickers hardness [16]. Because ultrasonic vibration can produce oscillating strain and stress fields in solid materials [17], some researchers have combined ultrasonic vibration with large plastic deformation technology to form new ultrasonic vibration-assisted large plastic deformation technology; this study found that ultrasonic vibration improves the processing results. F. Ahmadi et al. combined ultrasonic vibration with equal channel angular pressing (ECAP). The results showed that the grain size of the material processed by ordinary ECAP was refined to 45 μm . Ultrasonic vibrations with amplitudes of 2.5 μm and 5 μm were superimposed on ECAP, and the grains of the material were refined to 28.2 μm and 22 μm in one UV-ECAP process. The larger the amplitude is, the greater the degree of grain refinement and uniformity [18]. Liu et al. proposed using ultrasonic vibration-assisted upsetting to prepare nanostructured materials and found that the prepared material's grain size in the maximum deformation zone was refined to 100 nm [19]. Liu combined ultrasonic vibration and upsetting technology to process pure copper materials. Through simulation and experiments, it was found that the plastic deformation increased after superposing ultrasonic vibration. The processed pure copper material had a refined grain size of 50 μm to 100~300 nm [20]. Saeed Bagherzadeh et al. combined high-intensity ultrasonic vibration with ECAE technology and processed an Al1050 alloy. The study found that the application of longitudinal ultrasonic vibration and transverse ultrasonic vibration reduced the forming force by 30% and 14%, respectively.

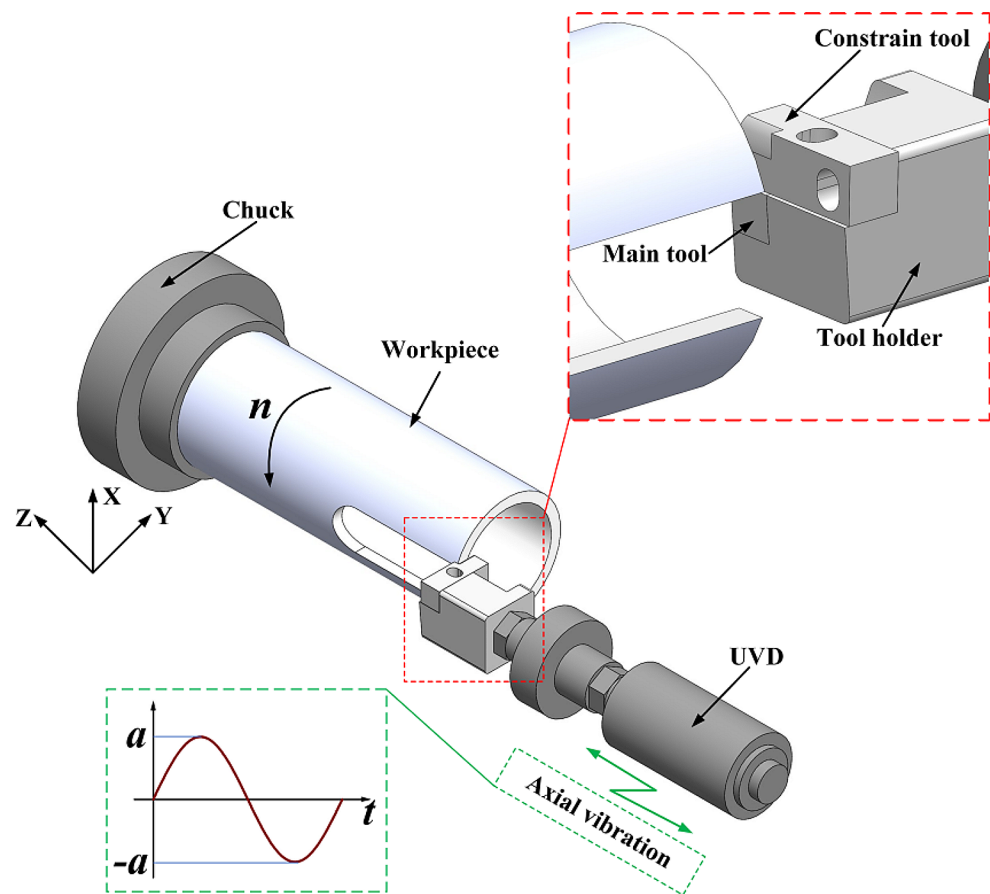
Under the condition that the average hardness of the initial specimen was 24 HV, the hardness of the material was 41 HV after one pass with ordinary ECAE, and the hardness of the material reached 47.6 HV after two passes. The hardness of the material obtained after ECAE with superimposed transverse ultrasonic vibration was 48 HV after one pass. The hardness of the material obtained after one pass with ECAE superimposed with longitudinal ultrasonic vibration was 51 HV. A 1050 aluminum alloy was processed by the longitudinal ultrasonic vibration ECAE method with an amplitude of 5 μm . After one pass, an equiaxed crystal with a grain size of 2 μm was obtained. The degree of grain refinement was higher than that of four passes of ordinary ECAE. The latter effect was even better [21]. Applying ultrasonic vibration to large plastic deformation technology can not only reduce the forming force, increase the hardness of the material, improve the uniformity of the material, and decrease the grain size but also reduce the number of processing passes, reduce repetitive labor, and considerably increase productivity. In the existing literature, there is little research on the combination of ultrasonic vibration and EC, and the processing mechanism and the influence of the processing parameters are unknown. This method has good research prospects and is worth exploring. Al6061 alloy is widely used in aerospace, construction, and transportation industries due to its good comprehensive performance, these applications put high requirements on its performance. When Al6061 alloy reaches the ultrafine-grained level, it shows high strength, high strain rate, sufficient ductility and good impact toughness, so it is chosen as the workpiece material.

This paper superimposes axial ultrasonic vibration and extrusion cutting processing technology to form a new processing technology based on existing research. The cutting principle is analyzed, and the equation of the tool cutting motion trajectory is established. The theoretical cut marks on the chip surface are predicted, and experimental verification is conducted. A comparative analysis of traditional EC and axial ultrasonic vibration-assisted extrusion cutting (AUV-EC) chip surface topography is performed under different tool rake angles, chip compression ratios, and cutting speeds. Comparison and analysis with and without axial ultrasonic vibration chip surface microstructures are conducted.

Analysis of AUV-EC principles

Figure 1 shows an illustration of AUV-EC. The tubular workpiece is clamped on the chuck of the lathe spindle. When the spindle rotates, the workpiece rotates with it. The three axes X, Y, and Z represent the cutting direction,

Fig. 1 Illustration of AUV-EC



radial direction, and feed direction (axial). The front end of the ultrasonic vibration device is connected to the combined tool with a threaded connection. The combined tool is assembled by the main tool, the constraint tool, and the tool holder. The ultrasonic vibration device can generate a vibration frequency of 33~34.5 kHz, and it is clamped on the tool holder. When the combined tool cuts the workpiece, the ultrasonic vibration device (UVD) makes the combined tool oscillate in the axial direction (feed direction), which means that the displacement in the axial direction of the combined tool is sinusoidal, as shown in Fig. 1.

In traditional EC, the main tool's movement trajectory and the cutting edge of the constraint tool in the XZ plane are straight lines. The chips become more regular after being squeezed by the channel and become usable strips. In AUV-EC, the main tool's movement trajectory and the constraint tool cutting edge in the XZ plane are not straight lines but sinusoidal curves (Fig. 1). Figure 1 shows that the combined tool generates axial ultrasonic vibration while cutting the workpiece.

Figure 2 shows the principle of AUV-EC. It can be seen that the workpiece moves along the X-axis in a uniform linear motion, and the main and constraint tools vibrate periodically along the Z-axis (feed direction). After the chips enter the extrusion channel, they are pressed by the main tool and

the constraint tool at high frequency and intermittently in the same direction and are then successfully squeezed out of the channel to produce a better quality strip. Because the axial ultrasonic vibration is superimposed, the surface of the chip will be cut to a specific regular surface topography before entering the extrusion channel. When passing through the channel, both the channel's squeezing action and the ironing action of the axial ultrasonic vibration change the formation principle of the chip strip. The surface topography and quality of the chip strip also change, which has particular research significance. In Fig. 2, γ_0 and α_{01} represent the rake angle and clearance angle of the main tool, α_{02} represents the clearance angle of the constraint tool, Φ represents the shear angle, t_d and t_{ch} represent the cutting thickness and chip thickness, respectively, and w represents the wall thickness of the pipe.

During AUV-EC, the direction of ultrasonic vibration is the feed direction (axial), so the cutting feed will change periodically. In the process of AUV-EC, the chips are simultaneously subjected to the dual effects of axial ultrasonic vibration cutting and axial ultrasonic vibration extrusion. In this article, to analyze the formation principle of the chip strip, it is simplified into two processes for analysis, namely, axial ultrasonic vibration cutting and axial ultrasonic vibration extrusion.

Fig. 2 The principle of AUV-EC

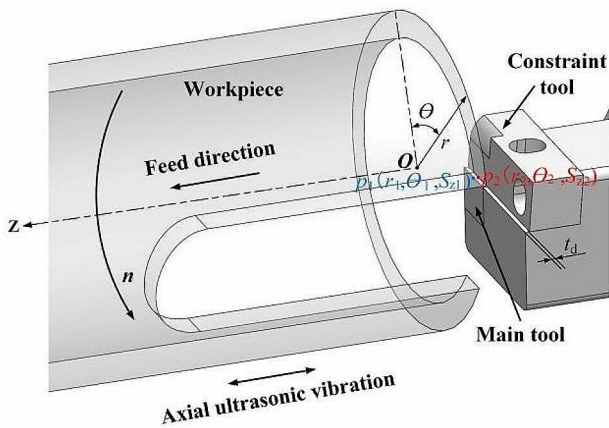
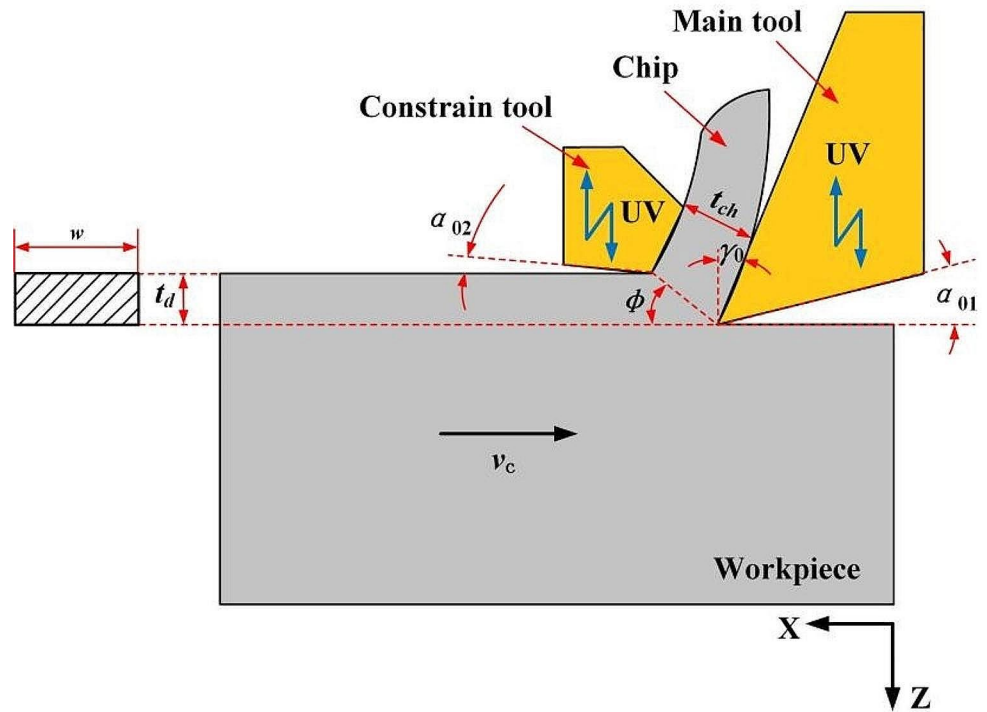


Fig. 3 Schematic diagram of AUV-LSEM process

Analysis of the axial ultrasonic vibration cutting process

Figure 3 is a schematic diagram of the AUV-EC, in which the coordinate axis Z has been established. Any point on the main tool and constraint tool's cutting edge can be selected to describe its motion path equation. Point p_1 on the cutting edge of the main tool in Fig. 3 can be expressed as [22]:

$$\begin{cases} r_1 = r_{p1} \\ \theta_1 = \omega_n t = \frac{n\pi}{30} \cdot t \\ S_{z1} = a \sin(\omega t) + t_d \end{cases} \quad (1)$$

Point p_2 on the cutting edge of the constraint tool can be expressed as [17]:

$$\begin{cases} r_2 = r_{p2} \\ \theta_2 = \omega_n t = \frac{n\pi}{30} \cdot t \\ S_{z2} = a \sin(\omega t) + t_d \end{cases} \quad (2)$$

where r_{p1} and r_{p2} are the cutting radii of points p_1 and p_2 on the cutting edge of the main tool and the constraint tool, respectively, S_{z1} and S_{z2} are the displacements of points p_1 and p_2 on the cutting edge of the main tool and the constraint tool along the feed direction (mm), respectively, θ_1 and θ_2 are the corners of points p_1 and p_2 on the cutting edge of the main tool and the constraint tool (rad), respectively, ω_n is the angular velocity of the spindle (rad/s), n is the speed of the main shaft (r/min), t_d is the cutting thickness (feed rate) (mm), ω is the circular frequency (rad/s), $\omega = 2\pi f$, f is the axial ultrasonic vibration frequency (Hz), and a is the ultrasonic amplitude (mm).

Replacing t with $\frac{30\theta}{n\pi}$ and ω with $2\pi f$, S_{z1} can be written as:

$$s_{z1} = a \sin\left(\frac{60f}{n} \cdot \theta\right) + t_d \quad (3)$$

S_{z2} can be written as:

$$s_{z2} = a \sin\left(\frac{60f}{n} \cdot \theta\right) \quad (4)$$

Formulas (3) and (4) show that after applying axial ultrasonic vibration, the cutting edges of the main tool and the constraint tool move intermittently in the axial direction, and their motion trajectories S_{z1} and S_{z2} are sinusoidal waveforms. When $2a < t_d$, Fig. 3(a) shows that the cutting motion of the main tool is continuous in a single cycle, and the cutting edge of the constraint tool does not contact the workpiece along AD; this is an intermittent motion. When $2a > t_d$, axial ultrasonic vibration cutting can achieve intermittent cutting [22]. As shown in Fig. 3(b), the main tool does not touch the workpiece in a single cycle along BC, which belongs to the uncutting stage. The constraint tool does not contact the workpiece along AD. Therefore, the combined tool is not in contact with the workpiece along BC. The cutting motion of the entire combined tool is a type of intermittent cutting. In this paper, to obtain a continuous chip strip with a regular shape, the cutting process of the main tool must be continuous, so $2a < t_d$ is required.

In formulas (3) and (4), the ratio of the vibration frequency f to the spindle speed n is set as the cutting frequency ratio W_f . The cutting frequency ratio can be divided into an integer part K and a fractional part δ , which can be expressed as [22]:

$$w_f = \frac{60f}{n} = \frac{f}{f_n} = K + \delta \tag{5}$$

The number of complete vibration cycles of the cutting edge of the constraint tool is determined by the integer K for each revolution of the workpiece. The fractional part δ is the remaining part of the vibration cycle, representing the vibration phase shift of two adjacent rotations and the positions of points p_1 and p_2 relative to the workpiece. If δ

is zero, the trajectories of the cutting edges of the adjacent rotating constraint tool are parallel, which means that the initial positions of the two motion trajectories are the same without phase shift. If δ is greater than zero, the trajectories of two adjacent rotations can intersect. This means that the initial phases of the two motion trajectories are different, resulting in a phase shift. The formula of the phase shift β is as follows [22]:

$$\beta = 2\pi\delta \tag{6}$$

In this paper, to obtain the chip strip, the cutting thickness t_d is between 0.4 and 0.8 mm, and the axial ultrasonic vibration amplitude a is between 1 and 8 μm . It can be seen that when $t_d \gg 2a$, the motion trajectory of the cutting edge of the main tool is continuous, and the motion trajectory of the cutting edge of the constraint tool is intermittent. Due to the large cutting thickness, the phase shift has little effect on the surface quality of the chip, so the influence of the phase shift is not considered. In the AUV-EC process, because the main tool edge and the constraint tool edge are not in the same plane (Fig. 1), the trajectories of the two are not necessarily parallel to each other during the cutting process. To simplify the geometric motion model, the elastic-plastic deformation of the workpiece material is ignored during the machining process and during friction and wear of the combined tool; it is assumed that the edge radius of the main tool and the constraint tool is 0, and the motion trajectories of the main tool and the constraint tool are set to be parallel, as shown in Fig. 4(a). In the actual machining process, the edge radius of the main tool and the constraint tool is not zero. In this article, if the radius of the edge is designed and processed to

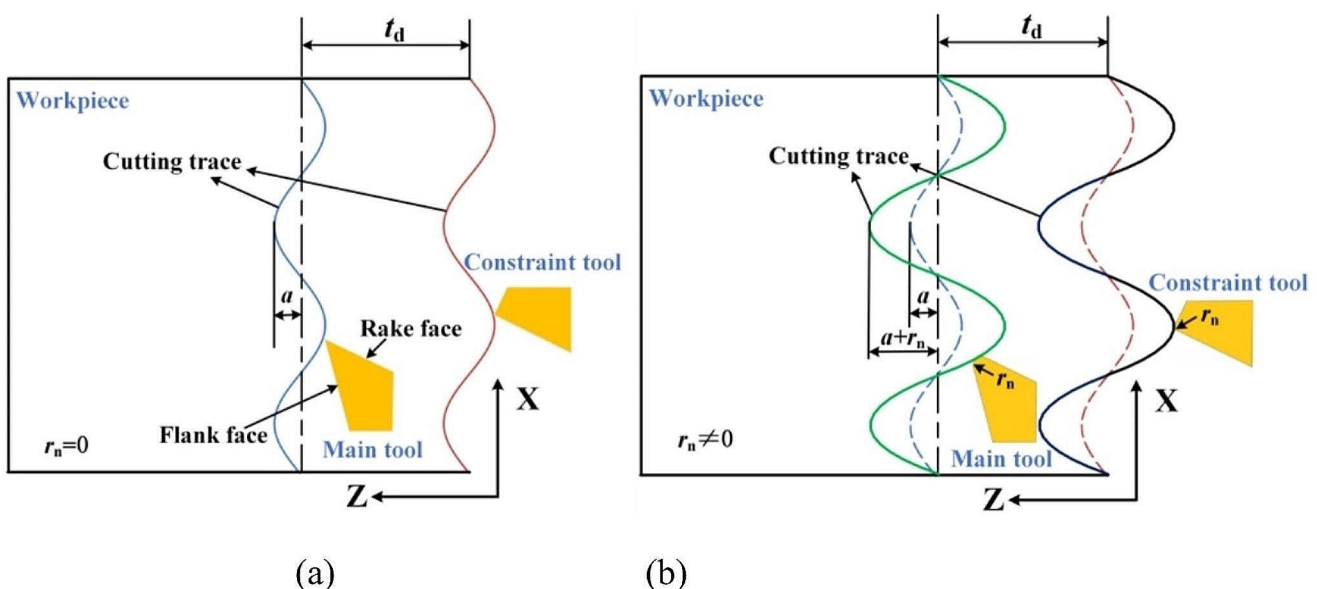


Fig. 4 The cutting motion trajectory of the main tool and the constraint tool

a value that is not zero, the cutting motion trajectory of the edge will change, as shown in Fig. 4(b).

Analysis of the axial ultrasonic vibration extrusion process

Similar to traditional EC, the chip thickness in AUV-EC depends on the chip compression ratio λ , $\lambda = t_{ch}/t_d$. During the machining process, axial ultrasonic vibration cutting is exerted first, and then axial ultrasonic vibration squeezing is performed. The chip surface close to the rake face of the tool is defined as the front side, and the other side is defined as the back side. To simplify the geometric motion model, ignoring the elastoplastic deformation of the workpiece material and the friction and wear of the combined tool during the machining process, after axial ultrasonic vibration cutting, the front and back of the chip will form a surface with a specific shape, as shown in Fig. 5(a)(b). The dotted line represents the theoretical cutting marks of the front and back. After entering the extrusion channel, the chip is subjected to the dual axial ultrasonic vibration squeezing action of the main tool and the constraint tool. The ultrasonic vibration extrusion channel has a certain ironing effect, which will change the cutting marks of the chip's front and back. As shown in Fig. 5(a)(b), the solid line represents the theoretical cutting marks of the chips after being extruded through the ultrasonic channel.

The dotted lines and solid lines in Fig. 5(a) are the theoretical surface cutting marks of the main tool and the constraint tool when the edge radius is $r_n=0$, before and after the chips enter the channel. The surface cutting marks of the chip before entering the channel are related to the amplitude, and the distance from the highest point of the protrusion and the lowest point of the recess to the horizontal line can be

approximated as the amplitude a . Due to the elastic-plastic deformation of the material itself, the cut chips become thicker. When the chip thickness compression ratio is less than the upper limit, the chips will fill the entire extrusion channel. At this time, the chips are squeezed in the channel while being pressed by the main tool, and the axial ultrasonic vibration of the constraint tool and the surface cutting marks of the chips will be affected. Moreover, because the ultrasonic amplitude of the main tool and the constraint tool remain unchanged, the cut surface can be approximated as flat, and the chip surface after extrusion is approximately flat. Figure 5(b) shows the theoretical surface cutting marks of chips before and after entering the channel when $r_n \neq 0$. Compared with Fig. 5(a), due to the influence of the edge radius of the cutting edge, the distance between the highest point of the convex and the lowest point of the recession and the horizontal line of the theoretical surface of the chip before entering the channel can be approximated as $a+r_n$. After the chips enter the channel, the surface cutting marks are squeezed while being ironed by axial ultrasonic vibration, and the distance between the protrusions and the recesses will be reduced. After extrusion, it can be approximated as r_n .

Experimental details

AUV-EC is performed on an ordinary lathe (C6240A), as shown in Fig. 6. The ultrasonic vibration device is clamped on a fixture base with a unique structure, and the ultrasonic generator provides energy. When the ultrasonic generator is started, the ultrasonic vibration device is driven to vibrate at a high frequency along the axial direction (feeding direction). After setting the parameters, this ultrasonic vibration

Fig. 5 Theoretical cutting marks on the chip surface

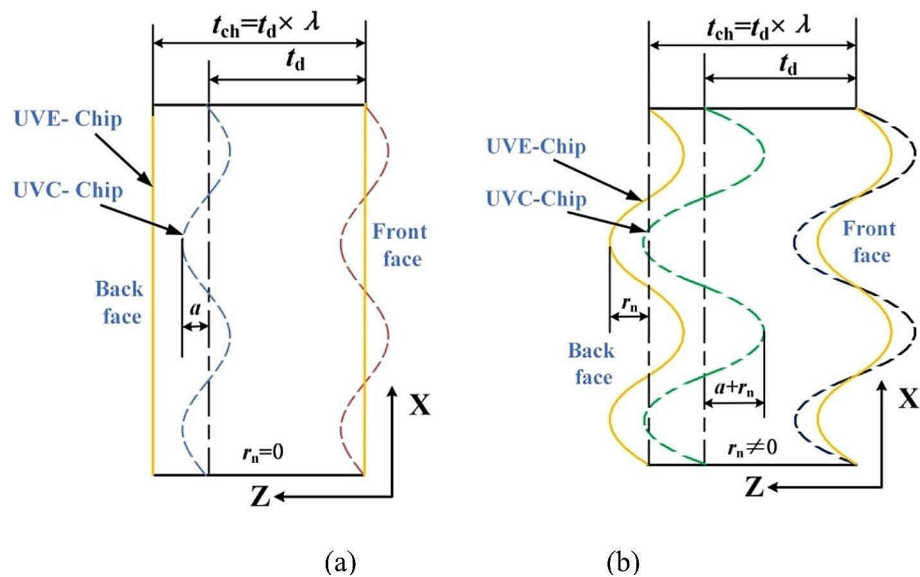
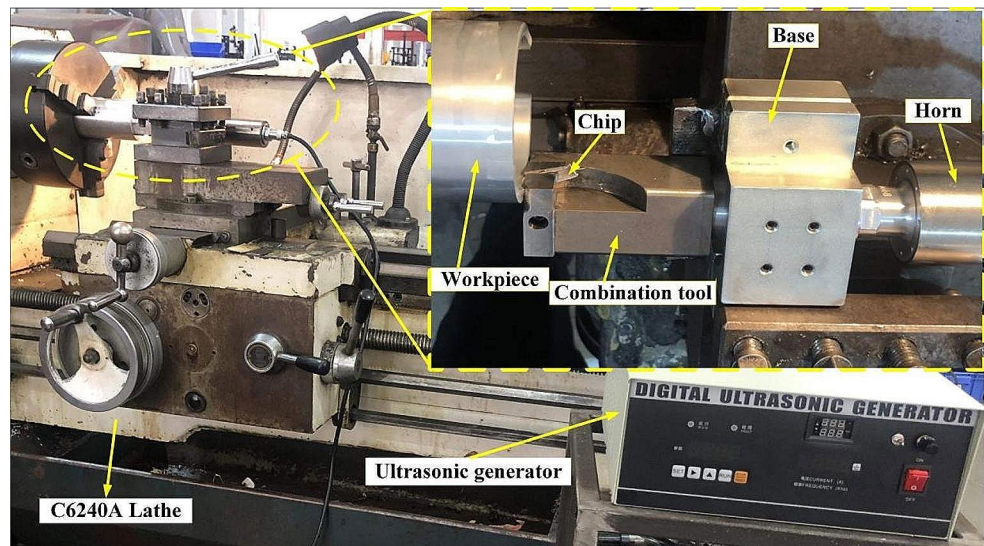


Fig. 6 Experimental setup for AUV-EC process**Table 1** The chemical composition of Al6061 alloy (wt%)

Element	Si	Fe	Cu	Mn	Mg	Cr	Zn	Ti	Al
Contents	0.40~0.8	0.7	0.15~0.40	0.15	0.8~1.2	0.04~0.35	0.25	0.15	balance

Table 2 Processing parameters of EC and AUV-EC

No.	Rake angle (°)	Chip thickness compression ratio	Cutting speed (mm/s)	Cutting thickness (mm)	Frequency (kHz)	Vibration amplitude (μm)
First group						
1	15					
2	20	1.75	92	0.6	0/33	0/3
3	25					
Second group						
4		1.25				
5	20	1.5	92	0.6	0/33	0/3
6		1.75				
7		2				
Three group						
8			92			
9	20	1.5	183	0.6	0/34.5	0/6
10			385			

device can output amplitudes of 1~6 μm and generate a resonance frequency of 33~34.5 kHz. The combined tool consisting of the main tool, the constraint tool, and the tool holder is fixed at the front end of the ultrasonic vibration device with screws. The clearance angle of the main tool and the constraint tool is designed and processed to 10°, and the cutting edge radius is designed and processed to 50 μm. The material of the main tool and the constraint tool is high-speed steel, and the material of the tool holder is 40Cr. The tubular Al6061 workpiece has an outer diameter of 70 mm and a wall thickness of 5 mm. Its chemical composition is shown in Table 1, and it is treated with T6. In this study, to verify the theoretical surface cutting marks of the chip

strip, a comparative analysis of the effects of the processing parameters in traditional EC and AUV-EC on the surface quality and microstructure of the chip strip was performed, and the processing parameters are shown in Table 2.

The prepared traditional EC and AUV-EC chip strip samples' surface topography were observed by optical profile (RTEC UP Dual Model, RTEC, USA), metallurgical microscope (DM2700M, Leica, Germany), and field emission scanning electron microscope (SEM) (SU8010, Hitachi, Japan). In order to count the surface grain size of the chip strip and obtain a high-definition image of the surface microstructure, the sample was polished with sandpaper and polished to 50 μm and then subjected to transmission

electron microscopy (TEM) observation after pre-thinning and ion thinning by electronic double spray. X-ray diffraction (XRD) (Ultima IV, Rigaku, Japan) was used to test the different phases of the samples.

Experimental results and discussion

The previous analysis shows that AUV-EC exerts the dual effects of axial ultrasonic vibration and extrusion on chips. Compared with traditional EC, the surface topography will be different. Figure 7 shows the front and back of the chip strip sample processed with the parameters numbered 5 in Table 2. Figure 7(a) is the front of the chip sample. The surfaces of the samples shown in the two pictures 7(a1)

and 7(a2) are relatively smooth, and there is no regular ultrasonic vibration cutting track. Figure 7(a3) shows the three-dimensional topography of the chip. It shows that the three-dimensional topography is almost all green except for a small amount of blue. This indicates that the surface is relatively flat and smooth, and the convex blue does not show any specific laws or present a regular ultrasonic vibration cutting track. After the chips enter the channel, due to the effect of the high-frequency axial ultrasonic vibration and the low speed, the ironing effect on the surface is improved, and the ultrasonic vibration cutting marks are eliminated.

Figure 7(b) shows the back of the chip sample. Compared with the front, the flatness of the surface is slightly reduced. Figure 7(b1) and 7(b2) are scanning electron microscope (SEM) images of the chips magnified 50 times and 500

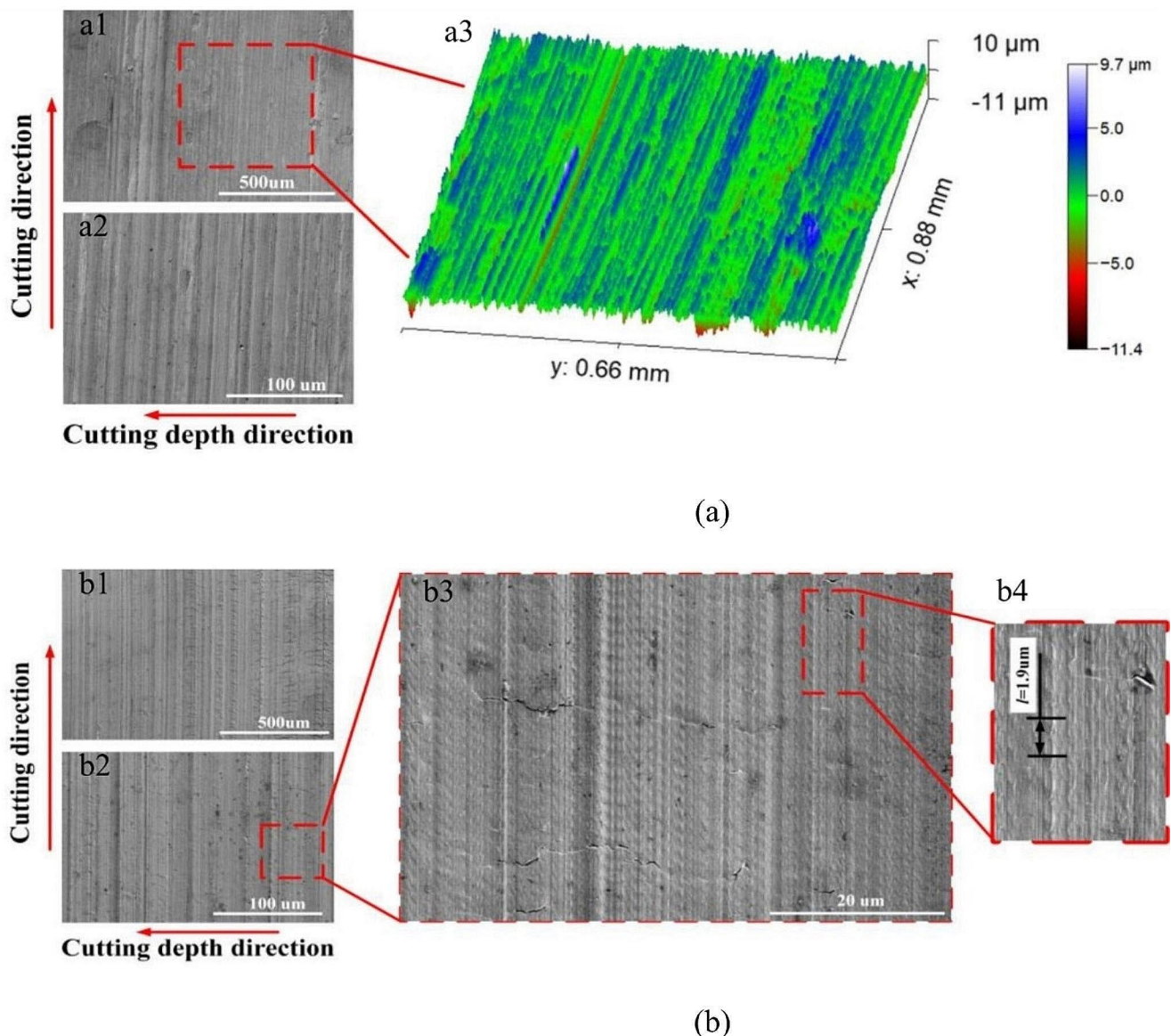


Fig. 7 The actual surface topography of No.5 sample: **(a)** Front; **(b)** back

times, respectively. The whole sample shows relatively regular cutting marks. Enlarging part of the red rectangular area in Fig. 7(b2) 2000 times, as shown in Fig. 7(b3), makes the surface cutting marks visible. Several regular cutting marks are arranged neatly along the cutting speed direction. This shows that the effect is not apparent after the chips enter the channel, although the cutting marks on the back are affected by ironing under the action of axial ultrasonic vibration extrusion. Therefore, the surface of the generated chip strip is relatively intact and retains the cutting marks before entering the extrusion channel. Comparing the front side and the back side of the chip strip, its appearance is entirely different. This is the front surface is a newly generated surface in contact with the main tool. Before entering the extrusion channel, the cutting marks partially rebound due to plastic deformation. After entering the extrusion channel, the rake face of the main tool rubs against the chips. Under the action of high-frequency axial ultrasonic vibration, the surface of the chip strip is ironed again, and finally, the cutting marks are almost eliminated. However, the back is the machined surface, which is in contact with the constraint tool. During processing, an indentation is formed by the constraint tool on the back of the chip. After entering the extrusion channel, the friction effect between the back of the chip and the constraint tool's contact surface is small. Under the action of high-frequency axial ultrasonic vibration, there is no substantial effect on the back of the chip. Therefore, a complete cutting trace is retained.

In the AUV-EC, the cutting marks on the chip surface are periodic (Fig. 4) [23]. The working time of one cycle is $1/f$; then, the theoretical wavelength l_t in one cycle is:

$$l_t = (1/f) * v_c \tag{7}$$

Sample 5 has an axial ultrasonic vibration frequency of $f=33$ kHz and a cutting speed of $v_c=92$ mm/s. Substituting the f and v_c values into formula (7) results in $l_t=2.79$ μm .

Ignoring the cutting marks on the chip surface, Fig. 8 shows the simplified model before and after the chip enters the extrusion channel. According to the principle of constant volume before and after cutting, this yields:

$$V_d = V_{ch} = l_1 * t_d * w = l_2 * t_{ch} * w \tag{8}$$

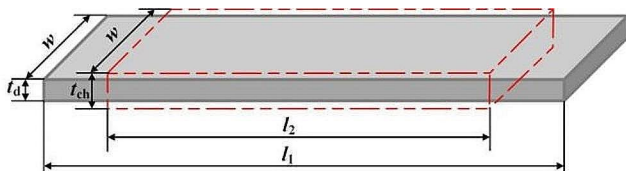


Fig. 8 Schematic diagram of chips before and after entering the extrusion channel

If both sides of the equation are reduced to w at the same time, this yields:

$$l_1 * t_d = l_2 * t_{ch} \tag{9}$$

$$l_2 = \frac{t_d}{t_{ch}} * l_1$$

$$l_2 = \frac{1}{\lambda} * l_1 \tag{10}$$

where l_1 and l_2 are the lengths before and after the chips enter the extrusion channel. Experiments have confirmed that the widths of the two are the same and remain unchanged with w . The other values are the same as before.

In the AUV-EC process, the change in the length of the chip before and after entering the channel affects the variation in the wavelength of the cutting trace. That is, the degree of wavelength change is consistent with the degree of change in the chip length, so formula (10) can be obtained:

$$l_e = \frac{1}{\lambda} * l_t \tag{11}$$

where l_e is the actual wavelength of a single cycle. For sample number 5, the compression ratio λ is 1.5. Substituting the λ and l_t values into formula (11) shows that l_e is 1.86 μm .

Part of Fig. 7(b3) is enlarged 5000 times, as shown in Fig. 7(b4). Through measurement, the wavelength l of a single cycle on the back of the chip is found to be 1.9 μm . $l \approx l_e$. This indicates that the theoretical cutting marks on the chip surface predicted previously are correct.

The influence of different processing parameters on the surface topography of the chip

As observed by the SEM, the surface quality of the Al6061 alloy chip strip processed by traditional EC and AUV-EC is significantly different, and the latter is much better than the former. The types of surface defects of the two kinds of chip strips are the same, but compared with the AUV-EC chip strips, the area and number of surface defects of the traditional EC chip strips are much larger. The types of defects are shown in Fig. 9 and mainly include tearing, scales, grooves, and cracks. Some chip surfaces have a small number of cavities and built-up edges [24, 25].

According to the previous analysis, the main tool cuts the workpiece to generate the front side of the chip strip, and the cutting edge of the constraint tool contacts the back side and exerts a force on the machined surface. Therefore, the topography of the front side and the back side of the

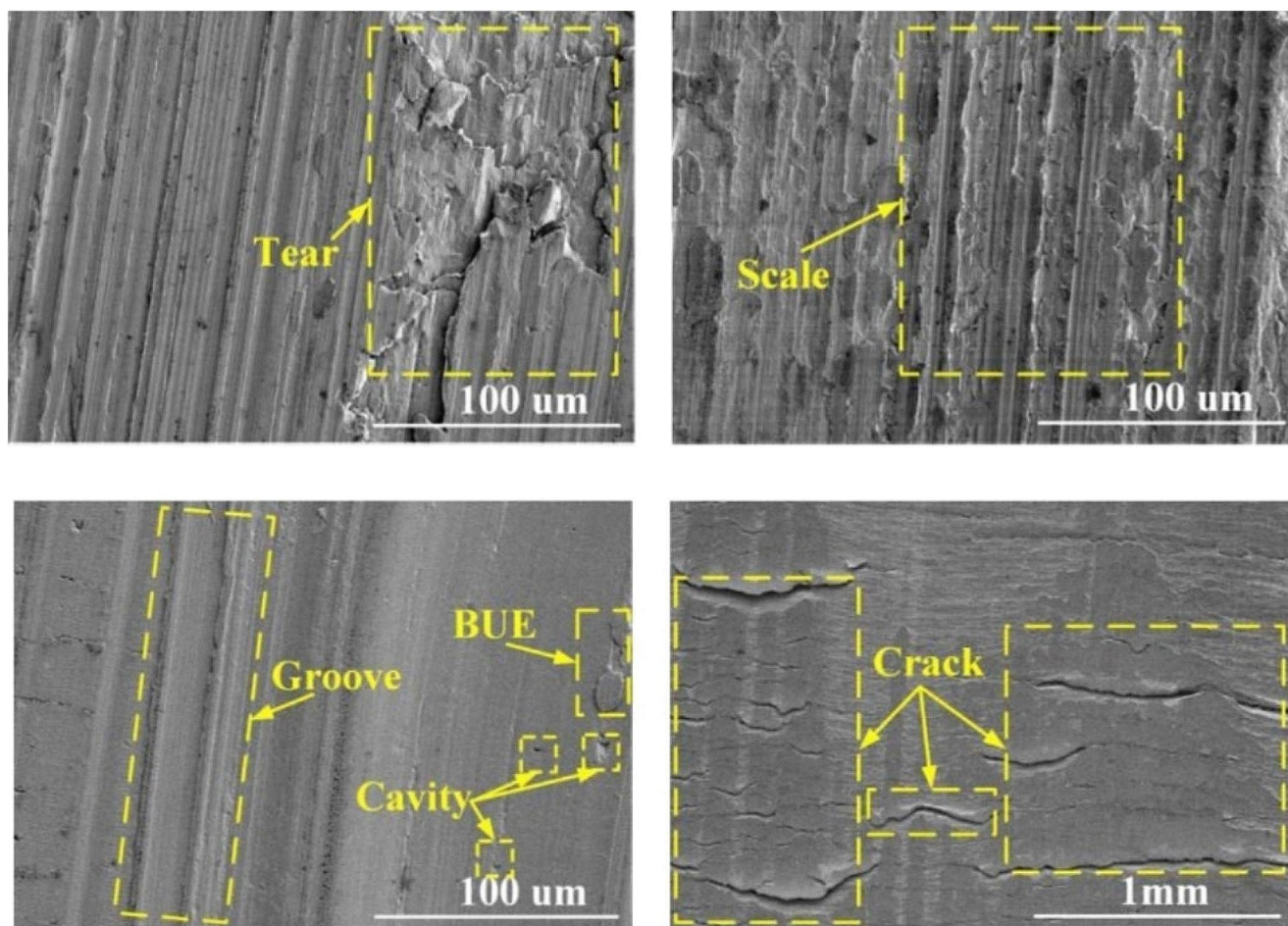


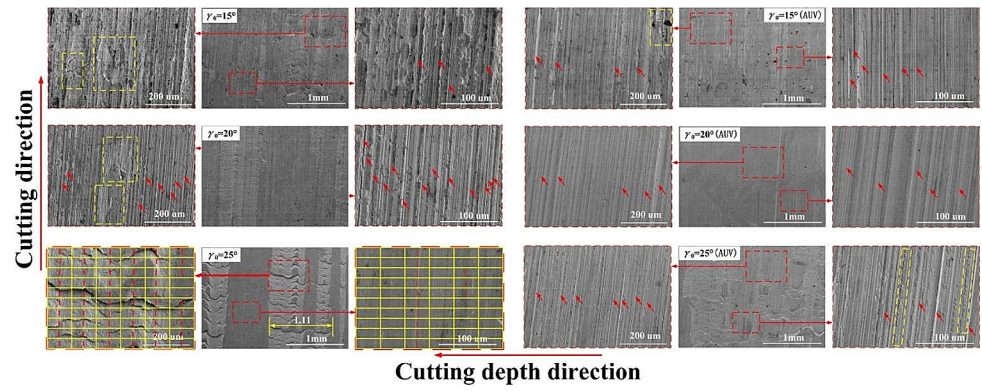
Fig. 9 Types of chip surface defects

chip are different, and the main surface defects will also vary. By observing the chip surface and back for all the processing parameters in Table 2, it is calculated that the main defects of the front side of the EC chip strip are tearing, scale, groove, and built-up edge. The AUV-EC chip strip has the first three types. For the front and back of the AUV-EC chip strip, there is no built-up edge, which shows that the axial ultrasonic vibration eliminates the built-up edge and improves the surface quality. In ordinary turning, the speed determines the generation of the built-up edge. The lower the speed is, the easier it is to generate a built-up edge. In traditional EC processing, the spindle speed is only 25 r/min, which is converted to a linear speed of 92 mm/s. When processing at this low speed, the built-up edge will inevitably appear on the surface of the chip strip. In the AUV-EC process, which is superimposed on the traditional EC, the chip formation mechanism is changed. Even at low speeds, the built-up edge can be reduced or eliminated, and the surface quality of the chip strip can be significantly improved [26].

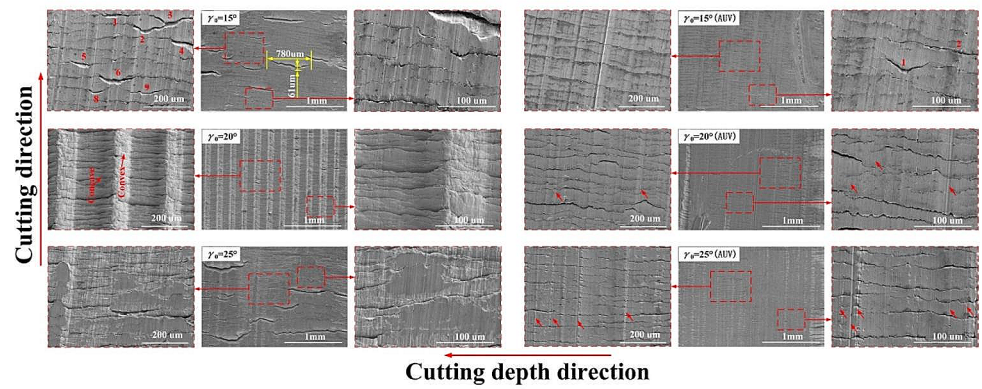
Influence of the tool rake angle

Figure 10 shows the surface topography of EC and AUV-EC chip strips under different tool rake angles. The quality of the front and back of the AUV-EC chip strip with different tool rake angles is far better than that of EC. Figure 10(a) shows the front topography of the chip strip. When the rake angle of the tool is 15° , the frontal defects of the EC chip strip are mainly scales, grooves (red arrow), and tearing. The scale covers almost the entire EC chip strip surface, and some areas even exhibit evident tearing phenomena (yellow dashed frame). When the cutting tool processes plastic materials at a low cutting speed, the oxide film and adsorption film on the rake face are wiped clean by the initially generated chips. It is difficult for lubricating oil and air to enter between the chip face and the rake face, so a new oxide film and adsorption film cannot be formed. Therefore, under the action of a large compressive stress, cold welding easily occurs between the newly generated chip face and the rake face, forming a cold welding knot, which prevents the flow of the chip. As the tool continues to cut, it will

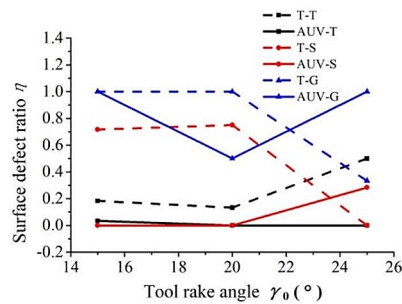
Fig. 10 Surface topography and surface defect ratio of EC and AUV-EC chips under different tool rake angles: **(a)(c)** Front side; **(b)(d)** backside



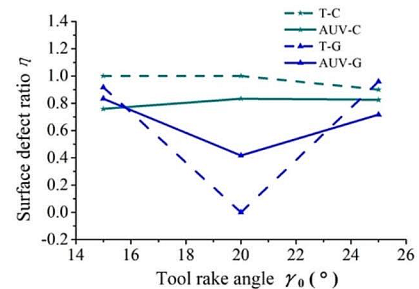
(a)



(b)



(c)



(d)

produce scales on the front face of the chip. Therefore, a large number of scales can be observed on the front of the EC chip strip. On the surface of the scales, due to the action of the main tool blade, there are many parallel grooves (red arrow). Compared with the EC chip, the AUV-EC chip strip looks smoother on the front, with relatively fewer surface defects, a small number of grooves and tears, and almost no scales. The main reason is that the constraint tool and the chip will separate periodically and momentarily under axial ultrasonic vibration. Air and lubricating oil flow between the back of the chip and the constraint tool while being sucked by the axial ultrasonic vibration between the chip's front

face and the rake face, forming a layer of oxidation film and adsorption film on the chip's newly generated surface and the rake face. The freshly formed oxidation film and adsorption film play the role of lubrication, destroy the conditions for the formation of cold welding, and eliminate the occurrence of cold welding, so this process is unable to generate scales. Comparing the surface groove defects of the EC and AUV-EC chip strips, the latter look more uniform and are smaller in number. The size and quantity of the tears in the local area of the AUV-EC chip strip are much smaller than those of the EC chip in the same test range. When the rake angle of the tool is 20°, the quality of the back of the EC

chip strip is slightly improved compared to 15°, and there are many fewer surface scale defects, but the tearing and groove defects are still clearly visible, and there is no reduction. The surface quality of the AUV-EC chip strip is dramatically improved compared with that at 15°. No scale or tearing defects can be seen at all, and fewer groove defects can be seen. Comparing the front topography of the EC and AUV-EC chip strips, it can be seen that the quality of the latter is far better than that of the former. The superposition of axial ultrasonic waves can reduce surface defects, especially scale and tear defects. When the rake angle is 20°, these two types of defect are almost eliminated. This is attributed to the superposition of axial ultrasonic vibration, which makes the constraint tool and the chips achieve intermittent contact, reduces the friction coefficient between the chips, and further reduces friction. In addition, the chips are pressed by high-frequency axial ultrasonic vibration after entering the extrusion channel, eliminating or repairing part of the surface defects and thus improving the surface quality [27]. This shows that the new process of AUV-EC can reduce subsequent processing of the strip by enhancing the surface quality of the chip strip. When the rake angle of the tool is 25°, the front topography of the EC and AUV-EC chip strips is not uniform, especially for EC. In the image magnified 50 times (1 mm), the transverse dimension of the longest tear is 1.11 mm. After the tearing defect in the local area is enlarged 200 times (200 μm), the tearing defect covers the whole picture, its size and number are large, and the tearing edge is very irregular. The grooves on the front of the AUV-EC chip strip are visible (red arrow), and there are a small number of scale defects (yellow dashed frame). The analysis concludes that the continued increase in the rake angle weakens the advantage of axial ultrasonic vibration. Compared with the 20° rake angle, the front quality is reduced, but it is still better than the front quality of the EC chip strip.

Figure 10(b) shows the topography of the back sides of EC and AUV-EC chip strips under different tool rake angles. The surface of the chip strip processed by different tool rake angles has no scale defects. Mainly due to EC processing or AUV-EC processing, the constraint tool does not cut to form a new surface, and its cutting edge only contacts the back of the existing chips, leaving tool marks. When the rake angle of the tool is 15°, the surface defects of the EC chip strip are mainly cracks and grooves. Along the cutting depth direction, there are multiple parallel groove defects. When it is magnified 200 times, nine larger cracks can be seen in the photographed area. The maximum crack size is 200×2 μm (length×width). When it is magnified 500 times (100 μm), many small cracks traverse the entire chip surface. Compared with EC chip strips, there are almost no large cracks on the back of AUV-EC chip strips magnified 50 times and 200 times, and only several smaller cracks can be seen. Two

relatively wide cracks can be seen at a magnification of 500 times. There are groove defects on the back of the chip strip, but the size and quantity are smaller than those of EC. The quality of the back of the AUV-EC chip strip is slightly better than that of EC. When the rake angle is 20°, the back side of the EC chip strip at a magnification of 50 times will show light and dark stripes of equal width and regular arrangement along the cutting direction. When magnified 200 times, the deep stripes are seen to be composed of numerous small concave cracks, and the light stripes are composed of numerous small convex cracks. At 500 times, small cracks are observed layer by layer and arranged together to form the back topography of the EC chip strip. This phenomenon is not observed on the back of the AUV-EC chip strip, which looks smoother at 50 times. When magnified to 200 times, many small cracks are arranged along the cutting direction, but the density is much smaller than that of EC, and there is no uneven topography. There are a small number of groove defects distributed on the surface (red arrow). Compared with the back of the EC chip strip, the AUV-EC chip strip has fewer defects and better quality. When the rake angle of the tool is 25°, the defects on the back of the EC chip strip are mainly cracks and grooves. Large cracks and small cracks are arranged irregularly on the back side, and several grooves arranged along the direction of cutting can be seen at 200 times and 500 times. There are no large cracks on the back of the AUV-EC chip strip at 50 times, but small cracks can be seen at the edges. When magnified to 200 times and 500 times, some small cracks arranged regularly along the cutting direction and grooves arranged along the cutting depth direction can be seen (red arrows). Comparing the back of EC and AUV-EC chip strips, the size and quantity of the former's cracks and grooves are larger than those of the latter, so the latter's quality is better than that of the former.

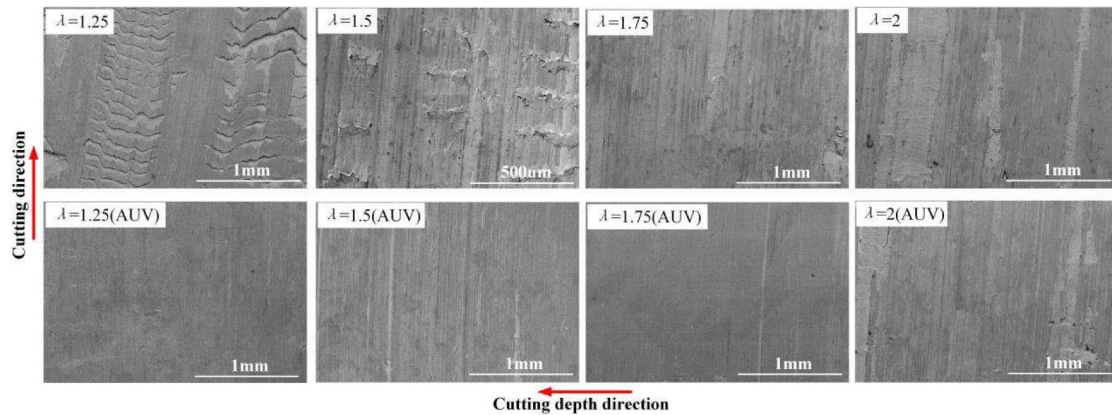
Because the surface quality of chip strips processed by traditional EC cannot be measured by roughness, this paper uses the surface defect ratio to evaluate the surface quality of EC and AUV-EC chip strips. The magnifications by 200 and 500 times of the shooting areas are divided into 60 rectangular grids, as shown in Fig. 10(a). The chip strip's surface defect ratio in the chip strip calculation formula is as follows [25]:

$$\eta = \frac{\sum_{i=1}^{60} N_i + \sum_{j=1}^{60} N_j}{120} \quad (12)$$

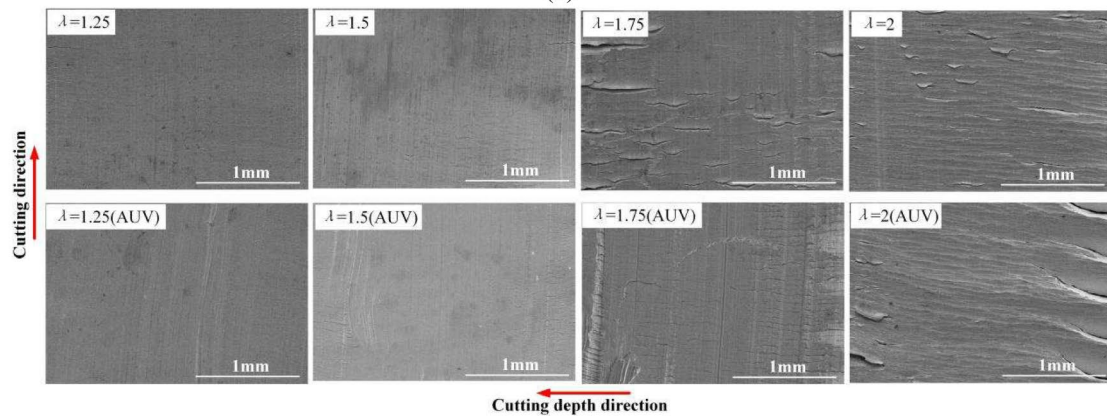
In the formula, N_i and N_j are the presence and absence, respectively, of surface defects of each rectangular grid in the shooting area magnified 200 and 500 times. When defects in the rectangular grid (such as tears and grooves) are detected, it is recorded as 1. The opposite is recorded as 0.

Figure 10(c)(d) shows the ratio of surface defects of EC and AUV-EC chip strips at different rake angles. T-T and AUV-T represent tear defects in EC and AUV-EC. The scale defects in EC and AUV-EC are T-S and AUV-S. T-G and AUV-G represent groove defects in EC and AUV-EC. T-C and AUV-C represent crack defects in EC and AUV-EC. When the rake angle of the tool is less than or equal to 20°, the ratio of all defects on the front side of the AUV-EC chip

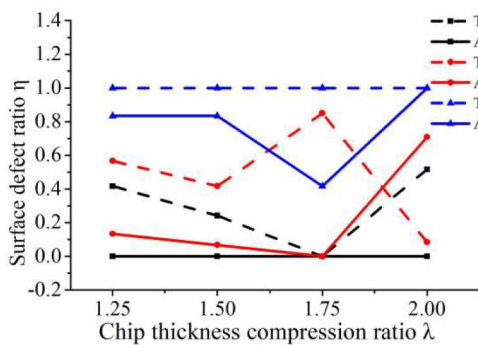
strip is less than that of EC. However, when the rake angle of the tool is equal to 25°, the ratio of scale and groove defects on the front side of the AUV-EC chip strip is greater than that of EC. This is because most of the front side of the EC chip strip is occupied by tearing defects, and other defects cannot be identified (Fig. 10(a)). When the rake angle of the tool is 15° and 25°, the ratio of crack and groove defects on the back of the AUV-EC chip strip is less than that of EC,



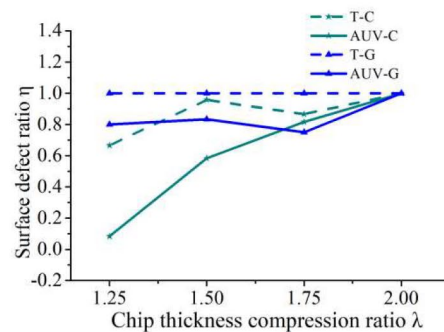
(a)



(b)



(c)



(d)

Fig. 11 Surface topography and surface defect ratio of EC and AUV-EC chips under different chip compression ratios: (a)(c) Front side; (b)(d) backside

but at 20°, the ratio of groove defects is larger than that of EC. This is because the back side of the EC chip strip is full of crack defects, the cracks are relatively large, and other defects cannot be distinguished (Fig. 10(b)).

When machining with different tool rake angles, the results show that the new processing technology of AUV-EC can weaken or even eliminate the shortcomings of the traditional extrusion cutting process, improve the surface quality of the chip strip, and reduce the chip strip's subsequent processing.

Influence of the chip compression ratio

Figure 11 shows the front and back topography of traditional EC and AUV-EC chip strips under different chip compression ratios. Figure 11a is the front topography of the chip strip. When the chip compression ratio is equal, the defects on the front side of the AUV-EC chip strip are much fewer than those of EC. When the chip compression ratio is less than or equal to 1.75, apparent tearing, scale, and groove defects can be seen on the front side of the EC chip strip, while only a few groove defects can be seen on the front side of the AUV-EC chip strip. The superposition of ultrasonic waves eliminates tearing and scale defects in traditional EC and improves surface quality. When the chip compression ratio is equal to 2, the surface topography of the AUV-EC chip strip is similar to that of EC. Because a chip compression ratio of 2 is close to the limit chip compression ratio of the Al6061 alloy, in this case, the combined tool has a small extrusion effect on the chips, which significantly weakens the effect of axial ultrasonic vibration on the chip surface, so the front surface of the processed chip strip is similar to that of the EC chip strip [28].

Figure 11(b) shows the topography of the back side of the chip strip. The primary defects are cracks and grooves. When the chip compression ratio is less than or equal to 1.5, the topography of the back side of the AUV-EC and EC chip strips is similar, but some small cracks can be seen in the latter. When the chip compression ratio is equal to 1.75, many large and small cracks can be seen on the back of the EC chip strip, while there are no large cracks on the back of the AUV-EC chip strip, only a few small cracks and a relatively prominent groove. When the chip compression ratio is equal to 2, the AUV-EC and EC chip strip's back topography is almost the same: full of large and small cracks. Since the effect of axial ultrasonic vibration is significantly reduced here, the impact on the back shape of the chip strip is almost absent. It can be seen that only when the chip compression ratio is less than or equal to 1.75 is the quality of the back side of the AUV-EC chip strip slightly better than that of EC.

Figure 11(c)(d) shows the ratio of surface defects of EC and AUV-EC chip strips under different chip compression ratios. Figure 11(c) shows that when the chip compression ratio is less than or equal to 1.75, the ratio of all defects on the front and back of the AUV-EC chip strip is less than or equal to that of EC. When the compression ratio is 2, the scale defect ratio on the front side of the AUV-EC chip strip is much greater than that of EC. Because most of the EC chip strip's front side is occupied by tearing defects, it is difficult to distinguish the scale defect. The ratios of the crack and groove defects of the two are equal. A chip compression ratio of 2 is close to the limit chip compression ratio of Al6061, so the compression effect of the combined tool on the chip strip is significantly reduced. This could weaken the influence of axial ultrasonic vibration, and the obtained surface topography is similar, so the defect ratio is also similar.

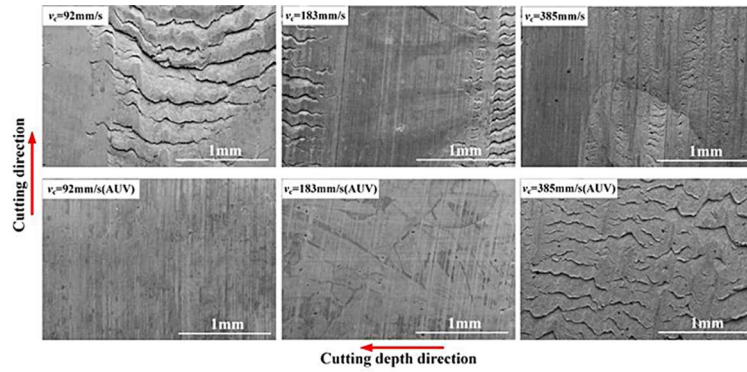
Influence of the cutting speed

Figure 12 shows the front and back topography of traditional EC and AUV-EC chip strips at different cutting speeds. Figure 12(a) is the front topography of the chip strip. When the cutting speed is less than or equal to 183 mm/s, the EC chip strip has many tear and groove defects on the front side, while AUV-EC results in only a few groove defects. When the cutting speed is equal to 385 mm/s, the tear size on the front side of the EC chip strip is reduced, while AUV-EC results in a large number of tear defects. This shows that when the cutting speed is high, the superposition of axial ultrasonic vibration not only does not improve but also accelerates the formation of surface defects.

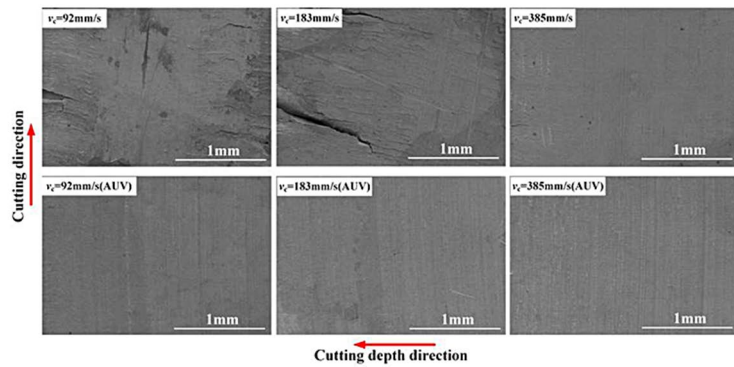
Figure 12(b) shows the topography of the back of the chip strip. When the cutting speed is less than or equal to 183 mm/s, more crack and groove defects can be observed on the back of the EC chip strip, while that of AUV-EC looks very smooth and flat with only a few groove defects. When the cutting speed is equal to 385 mm/s, there are crack and groove defects on the back of the EC and AUV-EC chip strips, and there are fewer crack defects on the surface of the EC chip. In summary, when the cutting speed is high, the effect of axial ultrasonic vibration on the improvement of groove defects on the back of the chip will be weakened, and crack defects will be aggravated.

Figure 12(c)(d) shows the ratio of the surface defects of EC and AUV-EC chip strips at different cutting speeds. When the cutting speed is less than or equal to 183 mm/s, the defect ratio of the front and back of the AUV-EC chip strip is much smaller than that of EC. When the cutting speed is equal to 385 mm/s, the ratio of crack and groove defects on the front of the AUV-EC and EC chip strips is relatively close, and the ratio of crack defects on the back of the AUV-EC chip strip is greater than that of EC. The

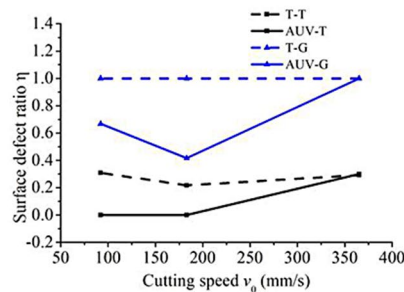
Fig. 12 Surface topography and surface defect ratio of EC and AUV-EC chips under different cutting speeds: (a)(c) Front side; (b)(d) backside



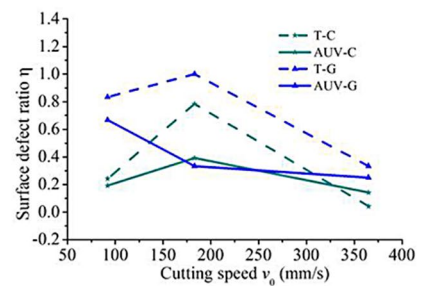
(a)



(b)



(c)



(d)

analysis concludes that due to the superposition of axial ultrasonic vibration, the constraint tool generates a high-frequency vibration on the back of the chip, causing vibration marks and cracks on the back of the chip. Due to the high cutting speed, the time for the back of the chip to undergo axial ultrasonic vibration ironing in the extrusion channel is extremely short. The cracks generated on the back of the chips cannot be repaired by high-frequency axial ultrasonic vibration ironing. In EC, the back side of the chip passes through the extrusion channel in a very short time and is only affected by the friction of the combined tool, resulting in fewer cracks. Therefore, the ratio of crack defects on the back side of the EC chip strip is slightly lower than that of AUV-EC.

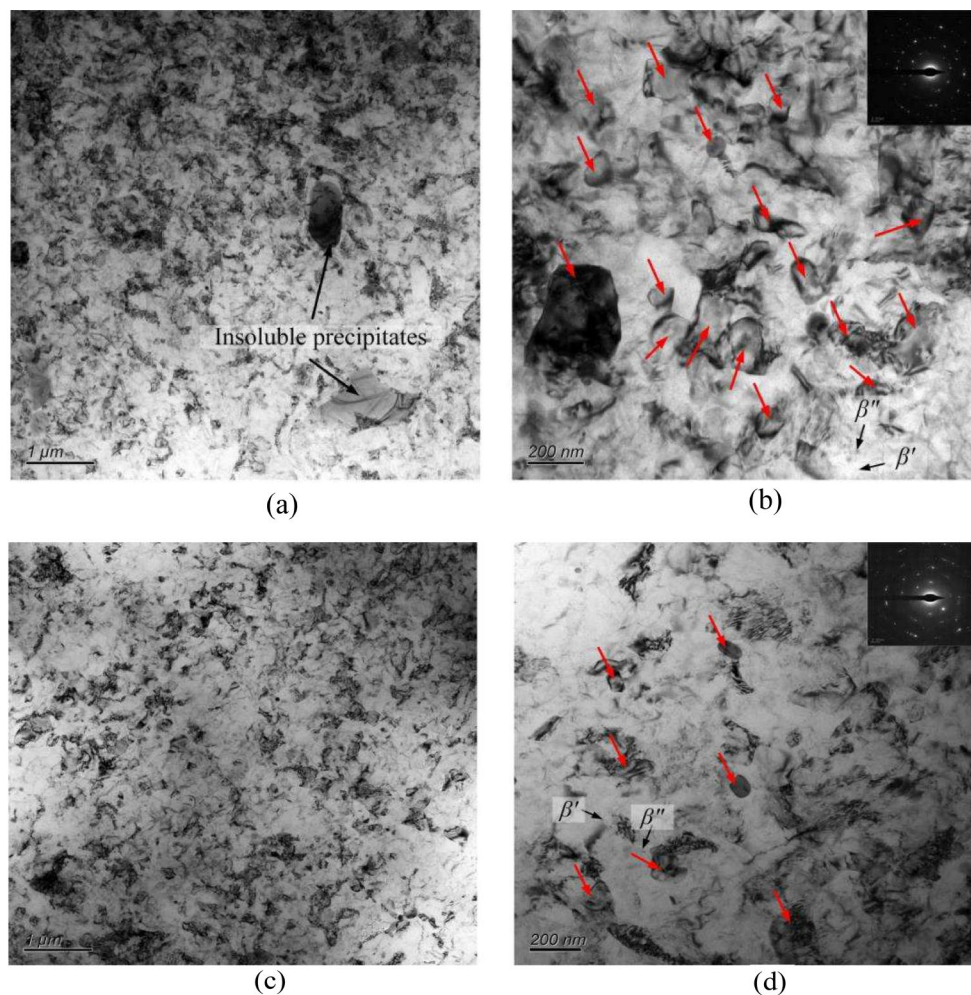
Microstructure of the chip

This paper uses only the 9th group of parameters in Table 2 as the research object for analysis in comparing the traditional EC and AUV-EC chip microstructures.

Microstructure

Figure 13 shows the transmission electron microscope image of the traditional EC and AUV-EC chip strips. Al6061-T6 tubular material is used, and the grain size is $\sim 75 \mu\text{m}$ [7]. Clearly, in the traditional EC and AUV-EC processes, large shear strains are generated inside the chips during processing, and the grain refinement effect is significant. In traditional EC, many dislocation entanglement areas can

Fig. 13 The microstructure of the Al6061 alloy after (a)(b) T6+EC; (c)(d) T6+AUV+EC



be found, and there are large-scale insoluble phases locally, as shown in Fig. 13(a). In Fig. 13(b), a relatively prominent stacking fault structure can be observed, the grain boundary is somewhat fuzzy, and a large number of dynamically recovered grains (red arrow) are distributed on the grain boundary [29]. The maximum size is approximately 404 nm, and some fine needle β'' (Mg_5Si_6) and spherical β' (Mg_2Si) secondary precipitates are dispersed in the matrix [30]. In AUV-EC, only a large number of dislocation entanglement areas can be observed. Compared with traditional EC, the dislocation entanglement is more evenly distributed inside the material, as shown in Fig. 13(c). Figure 13(d) shows that the stacking fault structure, dislocation entanglement, and grain boundary obtained through AUV-EC are more evident than those obtained through traditional EC. There are a few dynamically recovered grains (red arrows).

However, the size is small, the largest is approximately 277 nm, and fine needle β'' (Mg_5Si_6) and spherical β' (Mg_2Si) secondary precipitates can also be seen in the matrix. The average grain size of the sample is estimated by the linear intercept method. The average grain sizes of

traditional EC chip strips and AUV-EC chip strips can be obtained as 164 nm and 135 nm, respectively [31]. The analysis concludes that the superposition of axial ultrasonic vibration suppresses the dynamic recovery of crystal grains and improves the uniformity of dislocation distribution, thereby reducing the average grain size.

X-ray diffraction

Figure 14 shows the x-ray diffraction (XRD) patterns of the Al6061 alloy in different states. In the T6 sample, the number of β' (Mg_2Si) precipitated phases is smaller than the number of β'' (Mg_5Si_6) precipitated phases. This is mainly because the β'' precipitated phase is the main strengthening phase of the Al6061 alloy. In the cutting process, the β' peak becomes sharper, while the β'' peak becomes relatively blunt. At a cutting speed of 183 mm/s, large plastic deformation occurs inside the chip, and the friction between the chip and the combined tool during cutting and extrusion increases the cutting temperature to approximately 130 °C, which makes part of the β'' dissolve into the matrix and

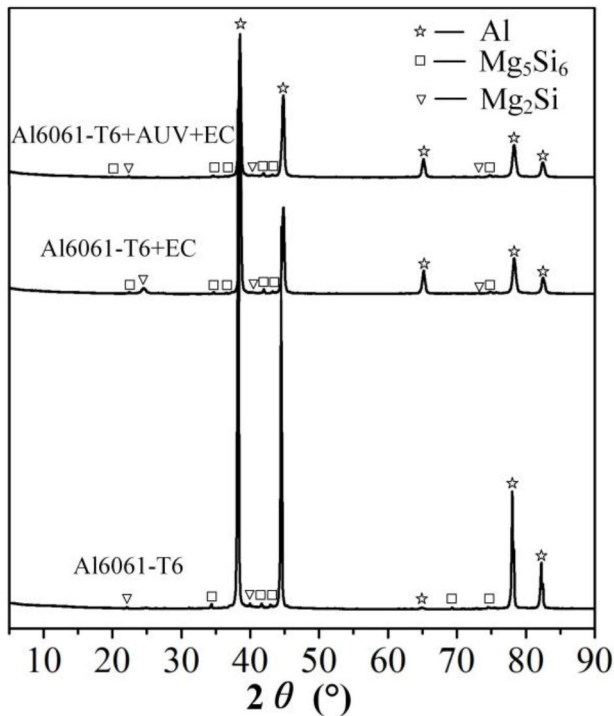


Fig. 14 X-ray diffraction patterns of the T6, T6 + EC, T6 + AUV + EC samples

promotes the precipitation of the β' phase. However, in the AUV-EC sample, the β' peak is more passivating than that of the EC sample, which indicates that the superposition of the axial ultrasonic vibration suppresses the precipitation of the β' phase. By calculation, the average grain sizes of EC and AUV-EC are 73.0 nm and 42.4 nm, respectively, reaching the ultrafine grain level, and the microscopic strains are 0.145% and 0.133%, respectively. Clearly, the average grain size of the chips in AUV-EC is smaller, which is consistent with the results of the previous analysis. The average grain size measured by XRD is smaller than the result measured by the transmission electron microscope (TEM). TEM analysis is usually more local and can only distinguish clear, large-angle grain boundaries. It is difficult to discriminate small-angle grains with small phase differences. However, XRD can analyze small-angle grain boundaries and sub-grain boundaries, so the measured size is smaller. Through derivation, the dislocation densities of EC and AUV-EC chips are found to be $2.57 \times 10^{14} \text{ m}^{-2}$ and $3.51 \times 10^{14} \text{ m}^{-2}$, respectively [32]. Clearly, there is a higher dislocation density in the chip after superposing axial ultrasonic vibration. This is mainly because the accumulation mechanism of the dislocation density changes under the action of axial ultrasonic vibration, which leads to the superimposed hardening effect, that is, the acoustic residual hardening effect [33], increasing the density of dislocations within the chips.

Conclusions

This paper proposes superimposing axial ultrasonic vibration based on traditional EC technology to form a new type of chip strip preparation technology and conducting experimental research on Al6061 alloys. By analyzing the processing principle of AUV-EC technology and comparing the surface quality and microstructure of AUV-EC and traditional EC chip strips, the following conclusions can be drawn:

- (1) AUV-EC is decomposed into axial ultrasonic vibration cutting and axial ultrasonic vibration extrusion for analysis. The motion trajectory equations of the main tool cutting edge and the constraint tool cutting edge are established, and the theoretical cut marks on the chip surface are predicted. The AUV-EC experiment shows that the actual cut marks on the chip surface are analyzed, and the correctness of the theoretical cut marks is verified.
- (2) Compared with the traditional EC process, the chip strip produced by the AUV-EC process under different rake angles, chip compression ratios, and cutting speeds has greater flatness and smoothness and lower surface defect ratios. This is due to the superposition of axial ultrasonic vibration. When the cutting speed is very low, ultrasonic vibration can eliminate or significantly reduce the surface scale and built-up edge phenomena that are common in traditional EC. Axial ultrasonic vibration enables the constraint tool to perform intermittent cutting and extrusion, preventing the formation of cold welding and reducing the friction coefficient between the cutting chips, thus improving the surface quality. In addition, after the chips enter the extrusion channel, the high-frequency axial ultrasonic vibration plays a role in ironing, which further reduces the chips' surface defects.
- (3) The surface grain refinement effect of traditional EC and AUV-EC chip strips is very significant. During processing, the chip produces a large shear strain, promoting the elongation and shearing of the grain. The traditional EC chip strip surface has a large insoluble phase. Many dynamic recoveries of crystal grains appear on the grain boundaries, and the maximum size is approximately 404 nm. However, only a small number of dynamically recovered grains are found on the chip surface of the AUV-EC, and the maximum size is only approximately 277 nm. The AUV-EC chip strip has a smaller average grain size than traditional EC. This result is confirmed in the XRD test.
- (4) Through XRD testing of Al6061-T6, Al6061-T6 + EC, and Al6061-T6 + AUV + EC, it is found that there are

β'' and β' precipitate phases in the three samples. In contrast to Al6061-T6, in the Al6061-T6 + EC sample, part of the β'' precipitated phase is dissolved in the matrix, and a new β' precipitated phase is formed. This phenomenon is not found in the Al6061-T6 + AUV + EC samples. Al6061-T6 + AUV + EC has a higher dislocation density than that of Al6061-T6 + EC, which is $3.51 \times 10^{14} \text{ m}^{-2}$.

Acknowledgements This work is supported by the National Nature Science Foundation of China (52105499).

Declarations

Competing of interest We wish to draw the attention of the Editor to the following facts that may be considered as declaration of interest statement and to significant financial contributions to this work.

We confirm that the manuscript has been read and approved by all named authors and that there are no other persons who satisfied the criteria for authorship but are not listed. We further confirm that all have approved the order of authors listed in the manuscript of us.

We confirm that we have given due consideration to the protection of intellectual property associated with this work. There are no impediments to publication, including the timing of publication, with respect to intellectual property. In so doing, we confirm that we have followed the regulations of our institutions concerning intellectual property.

The Corresponding Author is the sole contact for the Editorial process. She is responsible for communication with the other authors about progress, submissions of revisions, and final approval of proofs. We confirm that we have provided a current, correct email address accessible by Corresponding Author and has been configured to accept email from Measurement.

References

- Segal VM, Reznikov VI, Dobryshevshiy AE, Kopylov VI (1981) Plastic working of metals by simple shear. *Russ Metall* 1:99–105
- Bridgman PW (1952) Studies in large plastic flow and fracture, vol 177. McGraw-Hill, USA., New York. <https://doi.org/10.4159/harvard.9780674731349>
- Nath C, Rahman M (2008) Effect of machining parameters in ultrasonic vibration cutting. *Int J Mach Tools Manuf* 48(9):965–974. <https://doi.org/10.1016/j.ijmachtools.2008.01.013>
- Swaminathan S, Ravi Shankar M, Rao BC, Compton D, Chandrasekar W, King S, Trumble AH (2007) Severe plastic deformation (SPD) and nanostructured materials by machining. *J Mater Sci* 42:1529–1541. <https://doi.org/10.1007/s10853-006-0745-9>
- Iglesias P, Moscoso W, Mann J et al (2008) Production analysis of new machining-based deformation processes for nanostructured materials. *Int J Mater Form* 1(s1):459–462. <https://doi.org/10.1007/s12289-008-0094-0>
- Sevier M, Yang HTY, Moscoso W, Chandrasekar S (2008) Analysis of severe plastic deformation by large strain extrusion machining. *Metall Mater Trans A* 39:2645–2655. <https://doi.org/10.1007/s11661-008-9608-0>
- Bai X, Kustas A, Chandrasekar S, Trumble KP (2016) Large Strain Extrusion Machining on 6013 Aluminum Alloy. In *Light Metals*. 225–229. https://doi.org/10.1007/978-3-319-48251-4_38
- Iglesias P, Bermúdez MD, Moscoso W et al (2010) Influence of processing parameters on wear resistance of nanostructured OFHC copper manufactured by large strain extrusion machining. *Wear* 268(1):178–184. <https://doi.org/10.1016/j.wear.2009.07.009>
- Mert E, Moscoso W, Trumble KP et al (2012) Mechanics of large strain extrusion machining and application to deformation processing of magnesium alloys. *Acta Mater*. <https://doi.org/10.1016/j.actamat.2012.01.018>
- Klenosky DR, Johnson DR, Chandrasekar S, Trumble KP (2017) Characterization of large strain Extrusion Machining (LSEM) of AA7050. *Light metals* 2017. Springer Int Publishing 301–304. https://doi.org/10.1007/978-3-319-51541-0_40
- Wu YL (2017) The study of physicochemical properties and osseointegration of an ultrafine-grained titanium mini dental implant after morphology optimization [D]. Fourth Military Medical University
- Azushima A, Kopp R, Korhonen A, Yang DY, Micari F, Lahoti GD, Groche P, Yanagimoto J, Tsuji N, Rosochowski A, Yanagida A (2008) Severe plastic deformation (SPD) processes for metals[J]. *CIRP Ann* 57(2):716–735
- Ge Qiang E, Mostaed C, Zanella Y, Zhentao M, Vedani (2014) Ultra-fine Grained Degradable Magnesium for Biomedical Applications[J]. *Rare Metal Mater Eng* 43(011):2561–2566
- Kim WJ, Sa YK (2006) Micro-extrusion of ecap processed magnesium alloy for production of high strength magnesium microgears [J]. *Scripta Mater* 54(7):1391–1395
- Saldana C, Yang P, Mann JB, Moscoso W, Gill DD, Chandrasekar S, Trumble KP (2009) Micro-scale components from high-strength nanostructured alloys [J]. *Mater Sci Eng A* 503(1):17
- Yin XL, Deng WJ, Zou Y et al (2019) Ultrafine grained Al 7075 alloy fabricated by cryogenic temperature large strain extrusion machining combined with aging treatment. *Mater Sci Eng A* 138106. <https://doi.org/10.1016/j.msea.2019.138106>
- Shin SS, Kim WC, Kim KH et al (2015) Improvement of Riser Efficiency using high-intensity Ultrasonic Treatment in A356 Alloy. *Mater Trans* 56(9):1605–1608. <https://doi.org/10.2320/matertrans.M2015141>
- Ahmadi F, Farzin M, Meratian M et al (2015) Improvement of ECAP process by imposing ultrasonic vibrations. *Int J Adv Manuf Technol* 79(1–4):503–512. <https://doi.org/10.1007/s00170-015-6848-1>
- Liu YX, Suslov S, Han QY et al (2012) Microstructure of the pure copper produced by upsetting with ultrasonic vibration. *Mater Lett*. <https://doi.org/10.1016/j.matlet.2011.08.086>
- Liu YX, Han QY, Hua L et al (2013) Numerical and experimental investigation of upsetting with ultrasonic vibration of pure copper cone tip. *Ultrasonics* 53(3):803–807. <https://doi.org/10.1016/j.ultras.2012.11.010>
- Bagherzadeh S, Abrinia K, Liu Y et al The effect of combining high-intensity ultrasonic vibration with ECAE process on the process parameters and mechanical properties and microstructure of aluminum 1050. *Int J Adv Manuf Technol*, 2016:1–12, <https://doi.org/10.1007/s00170-016-8779-x>
- Zhang X, Sui H, Zhang D et al (2017) Feasibility study of high-speed Ultrasonic vibration cutting Titanium Alloy[J]. *J Mater Process Technol* 247(19):111–120
- Liu XF, Zhang JH et al (2019) Influence of tool material and geometry on micro-textured surface in radial ultrasonic vibration-assisted turning. *Int J Mech Sci*. <https://doi.org/10.1016/j.ijmecsci.2019.01.027>
- Razavi H, Nategh MJ, Abdullah A (2012) Analytical modeling and experimental investigation of ultrasonic-vibration-assisted oblique turning, part III: experimental investigation. *Int J Mech Sci*. <https://doi.org/10.1016/j.ijmecsci.2012.06.007>
- Chang L, Chengzu R, Guofeng W et al (2015) Study on surface defects in milling Inconel 718 super alloy. *J Mech Sci Technol*. <https://doi.org/10.1007/s12206-015-0345-1>

26. Muhammad R, Hussain MS, Maurotto A et al (2014) Analysis of a free machining $\alpha + \beta$ titanium alloy using traditional and ultrasonically assisted turning. *J Mater Process Technol* 214(4):906–915. <https://doi.org/10.1016/j.jmatprotec.2013.12.002>
27. Kumar VC, Hutchings IM (2004) Reduction of the sliding friction of metals by the application of longitudinal or transverse ultrasonic vibration. *Tribol Int* 37(10):833–840. <https://doi.org/10.1016/j.triboint.2004.05.003>
28. Kanani M, Sohrabi S, Ebrahimi R et al (2014) Continuous and ultra-fine grained chip production with large strain machining. *J Mater Process Technol* 214(8):1777–1786. <https://doi.org/10.1016/j.jmatprotec.2014.03.028>
29. Deshpande A, Tofangchi A, Hsu K (2019) Microstructure evolution of Al6061 and copper during ultrasonic energy assisted compression. *Mater Charact* 153. <https://doi.org/10.1016/j.matchar.2019.05.005>
30. Enayati HM, Abbasi-Baharanchi M, Karimzadeh F (2017) Mechanical and tribological behavior of severely plastic deformed Al6061 at cryogenic temperatures. *Mater Sci Engineering: A*. <https://doi.org/10.1016/j.msea.2016.11.099>
31. Liu HM, Cui H, Yang B et al (2004) Isothermal grain growth of reactive spray formed 7075 alloys in semi-solid state. *J Univ Sci Technol Beijing Mineral Metall Mater* 11(5):411–414. <https://doi.org/10.1080/02533839.2004.9670933>
32. Rokni MR, Widener CA, Champagne VK et al (2015) Microstructure and mechanical properties of cold sprayed 7075 deposition during non-isothermal annealing. *Surf Coat Technol* 276:305–315. <https://doi.org/10.1016/j.surfcoat.2015.07.016>
33. Messerschmidt U (2010) *Dislocation dynamics during plastic deformation*[M]. Springer, New York

Publisher's Note Springer Nature remains neutral with regard to jurisdictional claims in published maps and institutional affiliations.

Springer Nature or its licensor (e.g. a society or other partner) holds exclusive rights to this article under a publishing agreement with the author(s) or other rightsholder(s); author self-archiving of the accepted manuscript version of this article is solely governed by the terms of such publishing agreement and applicable law.